



HAL
open science

Early age autogenous shrinkage cracking risk of an ultra-high performance concrete (UHPC) wall: Modelling and experimental results

J. Kheir, A. Klausen, T.A. A Hammer, L. de Meyst, Benoit Hilloulin, K. van
Tittelboom, Ahmed Loukili, N. de Belie

► To cite this version:

J. Kheir, A. Klausen, T.A. A Hammer, L. de Meyst, Benoit Hilloulin, et al.. Early age autogenous shrinkage cracking risk of an ultra-high performance concrete (UHPC) wall: Modelling and experimental results. *Engineering Fracture Mechanics*, 2021, 257, pp.108024. 10.1016/j.engfracmech.2021.108024 . hal-03536712

HAL Id: hal-03536712

<https://hal.science/hal-03536712>

Submitted on 24 Jan 2022

HAL is a multi-disciplinary open access archive for the deposit and dissemination of scientific research documents, whether they are published or not. The documents may come from teaching and research institutions in France or abroad, or from public or private research centers.

L'archive ouverte pluridisciplinaire **HAL**, est destinée au dépôt et à la diffusion de documents scientifiques de niveau recherche, publiés ou non, émanant des établissements d'enseignement et de recherche français ou étrangers, des laboratoires publics ou privés.

1 Early Age Autogenous Shrinkage Cracking Risk of an Ultra-High

2 Performance Concrete (UHPC) Wall: Modelling and Experimental Results

3 J. Kheir^{1,2}, A. Klausen³, T.A. Hammer⁴, L. De Meyst¹, B. Hilloulin², K. Van Tittelboom¹, A.

4 Loukili², N. De Belie^{1,*}

5 ¹ Magnel-Vandepitte Laboratory for Structural Engineering and Building Materials, Ghent University,
6 Technologiepark Zwijnaarde 60, B-9052 Ghent, Belgium—e-mail: judy.kheir@ugent.be;
7 laurence.demeyst@ugent.be; kim.vantittelboom@ugent.be; nele.debelie@ugent.be

8 ² Institut de Recherche en Génie Civil et Mécanique (GeM), Ecole Centrale de Nantes, UMR-CNRS 6183, 1 rue de
9 la Noë, 44321 Nantes, France—e-mail: judy.kheir@ec-nantes.fr; benoit.hilloulin@ec-nantes.fr; ahmed.loukili@ec-
10 nantes.fr

11 ³ The Norwegian University of Science And Technology-NTNU, N-7491 Trondheim, Norway—e-mail:
12 anja.klausen@ntnu.no

13 ⁴ Architecture, Materials and Structures, SINTEF Building and Infrastructure, N-7465 Trondheim, Norway—e-mail:
14 torarne.hammer@sintef.no

15 * Corresponding author

16 Abstract

17 Ultra-High Performance Concrete (UHPC) exhibits high autogenous shrinkage (AS) which
18 significantly increases the risk of early age cracking. To predict the risks of early age shrinkage
19 cracking of environmentally friendly CEM III-based UHPC, a numerical model originally
20 developed for early age crack assessment of ordinary concrete, has been further developed and
21 applied on a demonstration wall with high risk of cracking, cast on a non-deforming slab. The
22 design of the wall was determined through numerical simulation using different parameters,
23 resulting from specific experiments performed on the desired concrete mixture. Early age crack
24 assessment parameters for the model were obtained through different tests performed using the
25 Temperature-Stress Testing Machine (TSTM). Finally, this UHPC wall was built, and occurring
26 strain deformations were recorded in real time using fiber optic (SOFO) sensors embedded in the
27 wall, and measurements taken from demountable mechanical strain gauges (DEMEC).
28 Restrained shrinkage measurements were obtained for the same mixture through ring tests. A
29 comparison between the numerical simulation results and the measurements proved that the
30 proposed model is suitable for UHPC, and the model predicts well the time of crack appearance.
31 Finally, it has been shown that shrinkage values along the wall height are influenced by the
32 degree of restraint.

33
34 **Keywords:** Ultra high performance concrete; modelling; early age crack assessment; autogenous
35 shrinkage; large-scale test

1. Introduction

Predicting the early age cracking risk of cementitious materials is a complicated and difficult task, since there are many properties involved, which develop very fast and highly influenced by temperature (i.e. from heat of hydration) and curing, especially for Ultra High Performance Concrete (UHPC) and High Performance Concrete (HPC). These concrete mixtures are known for their great mechanical and potentially high durability properties that are obtained due to their very low water to cement ratio, generally between 0.2 and 0.3 [1][2]. The high risk of early age cracking is the challenging issue in these durable concretes. Due to the low w/c ratio, UHPCs and HPCs undergo a high Autogenous Shrinkage (AS) driven by a self-desiccation that develops fast during the very early age (within the first days of age). AS, also known as autogenous deformation or basic shrinkage (Eurocode 2), is defined as the external macroscopical volume reduction that occurs under isothermal/sealed conditions, in other words it is the shrinkage that occurs when there is no temperature variation, volume change due to loss or absorbance of substances, or any application of external force [3]. During hardening, the internal relative humidity (RH) will drop and self-desiccation will occur if no external (or internal) water source is present. In mixtures with low water-to-binder ratios, water is rapidly consumed and a dense matrix is formed containing small pores. Hydrostatic tension forces (capillary forces) increase with the increase of smaller pores and lead to the increase in self-desiccation and autogenous shrinkage.. When it comes to UHPCs, RH drops rapidly in a short time to typically reach around 73% at 8 days and 68% after 3 months, while it was found to be 91% at 3 months for ordinary concrete [4]; these values will of course vary from one concrete to another. The previous statement implies that water/vapor filled pores are gradually emptied, and capillary tensions rise on the pore surface which is then perceived as autogenous deformations. As concrete is weak in tension at the early age, it is vulnerable for crack development resulting from high early AS [5][6]. These cracks impair the durability and the functionality of the UHPC structures by letting water with chemical agents and gases infiltrate inducing carbonation, steel corrosion, chemical attack and/or freeze-thaw damage [7]. Thus, in order to limit the cracking risk, it is very important to correctly estimate the evolution of the autogenous shrinkage [8].

Autogenous shrinkage can be measured on cement pastes, mortar and concrete using direct and/or indirect methods. The direct methods measure the volume or the linear autogenous

66 deformations whereas indirect methods measure in general the relative humidity or the porosity
67 of the cementitious material and correlations will be needed between AS and porosity or RH [9].
68 The buoyancy method, as developed by Loukili et al. [10], and the capillary tube method [11] are
69 used for volumetric autogenous measurements. Linear autogenous deformations rely on contact
70 and non-contact methods. The corrugated tubes method introduced by Jensen and Hansen [12] is
71 a contact method that combines volumetric and linear deformations with the ability to start the
72 measurement right after casting. Eddy current sensors and laser displacement sensors are
73 considered as non-contact methods for measuring autogenous shrinkage.

74 Different models were used to evaluate and predict autogenous shrinkage in HPCs. Tazawa and
75 Miyazawa [13] suggested a model that includes the product of the ultimate autogenous shrinkage
76 value, $\epsilon_{\infty}(w/cm)$, and coefficients $\beta(t)$ and γ , which describe respectively the development rate
77 of AS with time and the effect of cement type. Lee et al. [14] modified the previous model to
78 account for the AS strain that is contributing to the stress development, and applied it on
79 concrete containing mineral additives. Based on the pore structure of the concrete and the
80 capillary tension, Li et al. [15] created a prediction method of early AS of self-consolidating
81 concrete. Model B4 developed by Wan-Wendner et al. [16], is an improved model of the B3 one
82 [17] where prediction was expanded to modern concretes with numerous types of admixtures,
83 and mineral additions as well as the effects of various types of aggregates. Some of these
84 additions increase the shrinkage and creep and others decrease it. The important novelty of the
85 B4 model is the separation of autogenous shrinkage and drying shrinkage.

86 To predict the early age cracking behavior in massive concrete structures is still a difficult task to
87 perform, because of several complex coupling phenomena such as between the autogenous and
88 thermal strains. In a benchmark study done by Benboudjema et al. [18], different numerical
89 approaches were conducted on multi-scale models (micro- and macroscopic) to predict the early
90 age cracking behavior of a massive concrete structure in external restrained conditions. The
91 study concluded that at the macroscale, a thermo-activation method had to be used in the model
92 in order to have a satisfactory prediction of the adiabatic temperature; while a good prediction of
93 stresses can be achieved if the fast evolution of Young's modulus right after setting time can be
94 estimated. Other physically based numerical model approaches to predict shrinkage of structures
95 have been developed such as *fib* Model Code 2020, a developed version of *fib* MC2010 [19],
96 dealing with both new and existing concrete structures. Another key parameter when it comes to

97 restrained stress development and corresponding early-age cracking is the time dependent stress
98 response, hereafter denoted creep. Creep can significantly reduce AS- and temperature-induced
99 stresses at early ages: the literature shows a reduction of restrained stresses of as much as 30 –
100 50% due to the beneficial creep behaviour of concrete [18–21]. However, it should be noticed
101 that temperature-induced compressive creep at very early ages also can contribute to an increase
102 in the succeeding tensile stress development [22-23]. Because of the above described intricate
103 relations between early-age phenomena, an extensive knowledge is needed for the careful
104 calibration and development of models. This is particularly true regarding UHPC whose final
105 properties might considerably depend on their formulation and early age characteristics.
106 Therefore, coupled numerical and experience-based design methods would be particularly
107 beneficial in the scope of tailor-made cementitious materials and structures.

108 Various approaches at early-age cracking calculations are found in the literature [21], [26]–[33].
109 Some design approaches are merely an estimation of whether the concrete will crack or not,
110 while other and more complex approaches, chemomechanical [34] thermo-chemo-mechanical
111 [35] or hygro-thermo-chemo-mechanical approaches [36], also provide a prediction of the crack
112 development and the size and rate of occurring crack widths [37]. For all such early-age crack
113 assessments, the accuracy of the outcome is very dependent on the quality and correctness of the
114 models and material parameters used as input [23], [38]–[42]. In the current study, a pragmatic
115 “to crack, or not to crack”-approach was applied [43] by using the special-purpose program
116 CrackTeSt COIN [44]. This approach is considered accurate and advanced, but still practical and
117 easy applicable for contractors and structural designers [45]. In the current study, an early-age
118 crack assessment on a typical restrained wall was performed in CrackTeSt COIN to assess and
119 predict the cracking risk. The model was also used to further determine the conditions necessary
120 to achieve cracking at a specific point of interest in time, around 20 hours after water addition.
121 The combination of a thin wall cast on a stiff base was selected, since this would best provoke
122 cracks by early age shrinkage. The wall was kept thin to minimize the influence of temperature
123 related deformations, and the use of fibres was omitted. The same wall design could then
124 afterwards be used to test the effectiveness of internal curing agents such as superabsorbent
125 polymers to avoid early age cracks. Parameters for the model were obtained through different
126 tests including a test in a Temperature-Stress Testing Machine (TSTM). Then a wall has been
127 built in order to verify the simulated cracking risk through visual observation and deformation

128 measurements. The real-time occurring strains were recorded automatically with the use of
129 embedded fiber optic sensors and manually with mechanical demountable strain gauges through
130 measuring points glued on the wall. In addition, ring tests were carried out to measure restrained
131 shrinkage, and concrete mechanical properties such as compressive strength and E-modulus were
132 determined.

133 **2. Materials and methods**

134 **2.1. Concrete characterization**

135 **2.1.1. Introduction**

136 The current sub-section describes the first part of the study: determination of parameters
137 necessary to conduct early age crack assessment of the given concrete. The currently applied
138 methodology for parameter characterization has been verified and thoroughly described in [43].
139 The results presented in the current section were used to create a material database file
140 representing the given concrete for implementation in CrackTeSt COIN (CTC) [44], where CTC
141 is a two-dimensional special-purpose program for early age crack assessment.

142 **2.1.2. Concrete mix design**

143 The concrete mix design was determined after various optimisation steps, starting from a
144 previously reported mix design [46]. This initial mix design was adapted to the Norwegian
145 situation and made with local Norwegian ingredients (such as aggregates of size 0-8 mm, which
146 are typical in Norway). A blast furnace slag cement CEM III/A 52.5 R (Dyckerhoff Variodur 40)
147 was used in the mix with a dry undensified silica fume (19.8% by weight of cement), and a
148 limestone filler with a quantity of 23.8% by weight of cement. The superplasticizer ViscoCrete
149 UHPC-2 with 40% of active compound was used with a dosage of 1.4% by weight of cement;
150 the water to binder ratio (w/b) equaled 0.2. In the majority of UHPC applications fiber
151 reinforcement is known to be present. In this study, fibers were not used since it was not our goal
152 to increase the flexural or tensile strength. Besides, the mixture design of this study was part of a
153 project [47] where the main focus was rather on the improvement of the matrix itself by internal
154 curing agents known as SAPs (superabsorbent polymers) to achieve crack resistance properties.
155 Three batches were mixed out of the composition shown in Table 1, batches A, B and C. Batch A
156 was used to determine the hydration heat evolution of the cement, batch B was used to assess

157 the compressive and tensile strength development, and batch C was used for tests in the Free-
158 Deformation (FD) and the Temperature-Stress Testing Machine (TSTM) systems.

159 Table 1: Concrete mix design

Materials	(kg/m³)
Sand 0/4	401.9
Basalt 4-8 mm	649.3
Silica Fume - Elkem Microsilica 940 U	153.8
Cement - Variodur 40 (CEM III/A 52.5 R)	778.2
Filler - Betofill VK50 (limestone)	185.5
Water	186.4
Superplasticizer-SIKA Viscocrete UHPC-2	11.2

160

161 **2.1.3. Testing of Concrete**

162 2.1.3.1. Hydration heat

163 Semi-adiabatic calorimeter tests were performed in a NTNU-box (15 L samples) in order to
164 determine the hydration heat evolvement of the concrete. The NTNU-box comprises a plywood
165 box insulated by 100 mm Styrofoam (with known thermal properties) on all sides. During
166 testing, the box was stored in air at 38 °C while the air and concrete temperature were measured
167 continuously for 4 days.

168 2.1.3.2. Strength and E-modulus

169 Compressive strength tests were performed on triplicate 100x100x100 mm³ cubes according to
170 NS-EN 12390-3:2009 [48]. Uniaxial tensile strength tests were performed on triplicate
171 100x100x600 mm³ prisms (without notch) in an INSTRON 5985 electromechanical testing
172 system [49], the test set-up is described by Klausen et al. [43]. The main focus in the current
173 study has been early age cracking, and in this perspective, the elasticity modulus in tension is the
174 main parameter. The tensile E-modulus was found from the load-deformation relation measured
175 in the uniaxial tensile strength tests, where the E-modulus was deduced as the stress/strain ratio
176 between 10% and 40% of the failure load.

177 **2.1.4. Model equations and parameters**

178 The maturity principle was applied to describe the effect of curing temperature on the heat and
 179 property development of the given concrete. The Arrhenius equation was used as temperature
 180 function, and the rate of hydration $H(T_i)$ could consequently be expressed as given in Eq. 1.
 181

$$H(T_i) = \exp\left\{\frac{E_T(T_i)}{R} \cdot \left(\frac{1}{293} - \frac{1}{273 + T_i}\right)\right\} \quad \text{Eq. 1}$$

182 Where: R (J/(K.mol)) is the gas constant, T_i (°C) is the temperature and E_T (J/mol) is the activation
 183 energy: $E_T = A + B(20 - T_i)$, A (J/mol) and B (J/(K.mol)) are model parameters, where B = 0 for $T > 20$ °C
 184 and B has a given value for $T < 20$ °C
 185

186 The increase in maturity within a time increment is then $H(T_i) \cdot \Delta t_i$, while the maturity time at a certain
 187 concrete age is the sum of all maturity growth increments. For the given concrete, the activation
 188 energy parameters A and B were assumed based on experiments with previous concretes having
 189 similar properties [50], see Table 2.

190 The development of compressive strength, tensile strength and E-modulus in tension were
 191 modelled by a modified version of the CEB-FIP MC 1990 model, Eq. 2 [51]–[53]. For each
 192 property, the model was fitted to the test results by using the method of least squares. The
 193 obtained model parameters are presented in Table 2, and illustrated in Figure 3.
 194

$$X(t_e) = X(28) \cdot \left\{ \exp \left[s \cdot \left(1 - \sqrt{\frac{672 - t_0}{t_e - t_0}} \right) \right] \right\}^n \quad \text{Eq. 2}$$

195 Where $X(t_e)$ is the property as a function of maturity t_e (MPa if X is equal to f_c or f_t and GPa if it is equal
 196 to E), $X(28)$ is the property at 28 days, s and n are unitless curve-fitting parameters (the s-parameter is the
 197 same for all properties, while the n-parameter is varying), and t_0 is the starting time for stress
 198 development [maturity hours] found from the TSTM-test.
 199
 200

201 Table 2: Model parameters obtained by using the method of least squares for all tested ages

A	B	t_0	s	n_c	n_t	n_E	f_{c28}	f_{t28}	E_{28}
[J·mol ⁻¹]	[J·mol ⁻¹ ·K ⁻¹]	[h]					[MPa]	[MPa]	[GPa]

45000	400	8.0	0.141	1.000	0.744	0.323	151.2	6.7	42.8
-------	-----	-----	-------	-------	-------	-------	-------	-----	------

202

203 **2.1.5. Testing in the FD and TSTM systems**

204 The currently investigated concrete was tested in the Free-Deformation (FD) system and the
 205 Temperature-Stress Testing Machine (TSTM) system. The test set-ups and procedures for these
 206 systems are thoroughly described and illustrated in [43], [54], [55].

207 In the FD system, the autogenous shrinkage of two horizontally oriented and sealed specimens
 208 with dimensions of 100x100x500 mm³ was measured. The FD system is temperature-controlled,
 209 and the specimens were exposed to 20 °C isothermal conditions during testing. The length
 210 measurements were initiated approx. 2 hours after mixing. Autogenous shrinkage was measured
 211 up until 289 hours (12 days), and all measurements were zeroed at the starting time for stress
 212 development, $t_0 = 8$ hours (found from the TSTM test).

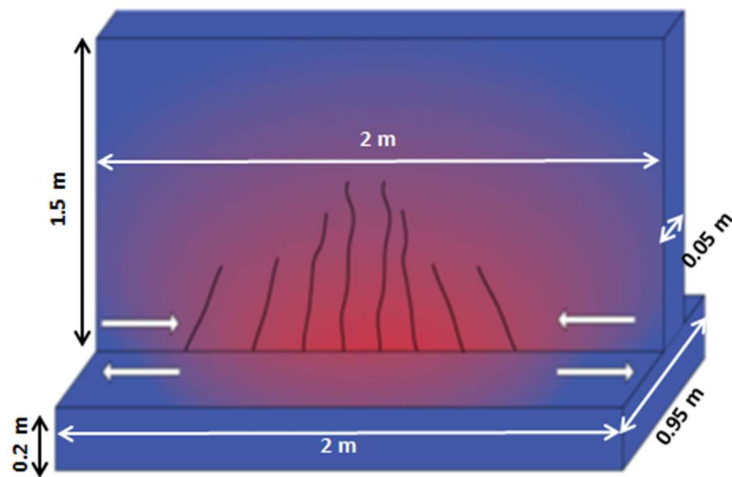
213 The TSTM system consists of a dilation rig and a Temperature-Stress Testing Machine (TSTM).
 214 The dilation rig measures the free deformation of a horizontally oriented specimen with
 215 dimensions of 100x100x500 mm³, while the TSTM is constructed to measure the restrained
 216 stress development in the hardening phase for a given degree of restraint. For both rigs, the
 217 concrete specimens were carefully sealed with plastic sheets and aluminum foil to prevent any
 218 water loss during testing. The TSTM system is temperature-controlled, and the specimens were
 219 subjected to a realistic temperature history representing a 50 mm thick concrete wall cast under
 220 Norwegian summer conditions, i.e. ambient temperatures of 20 °C.

221 **2.2. Large-scale demonstration wall**

222 **2.2.1. Concrete mix design and mixing procedure**

223 Based on the modelling results in section 3.1, the demonstration wall was cast as seen in Figure 1
 224 with the following dimensions: the slab was 2 x 0.95 x 0.2 m³ (l x w x t), and the wall was 1.5 x
 225 2 x 0.05 m³ (h x l x t). To limit the influence of heat produced by the exothermic hydration
 226 reaction of cement, the thickness of the wall was kept limited. This was done to minimize the
 227 influence of thermal contraction caused by cooling beyond the hydration heat peak, and of
 228 thermal gradients which could lead to thermal cracking. The slab was reinforced with two
 229 reinforcement meshes (150 mm) of diameter 8 mm positioned with a minimum concrete cover of
 230 25 mm, and the wall with a steel mesh of mesh size 150 mm and diameter 5 mm positioned in

231 the middle of the wall. The slab-wall connection was created using a 1200 mm long steel mesh
 232 with a height of 60 mm (mesh size 10 mm and diameter 2 mm) introduced in the slab for 50 mm
 233 along the length of the wall and two reinforcement bars (diameter of 12 mm and total length of
 234 300 mm), each located at 75 mm from one of the ends. The mesh and the reinforcement bars
 235 were placed in the slab by sawing a groove and drilling two holes and subsequently gluing them
 236 with epoxy.



237
 238 Figure 1: Schematic representation of the demonstration wall and its dimensions

239 The mix design of the traditional concrete of the slab and mixing procedures of the concrete of
 240 both the slab and the wall can be found in

241 Table 3 and Table 4. The mix design of the concrete wall is the same as shown in Table 1. It
 242 should be noted that the amount of superplasticizer used (1.1 m% by weight of cement) was less
 243 than that used in the batches for the modelling (1.4 m% by weight of cement) to obtain the same
 244 slump flow value (700 mm). The slab was cast 3 months prior to the wall and stored at ambient
 245 temperature ranging between 7 °C to 22 °C, to ensure that the influence of remaining drying
 246 shrinkage of the slab could be neglected in the time period considered. The concrete of the slab
 247 and the wall were each mixed using a rotating pan mixer Zyklos from the company Pemat-
 248 Germany with a capacity of 200 L, a speed of 46 rpm for the rotation of the mixing blades and
 249 189 rpm for the pan.

250 Table 3: Mix design composition of the slab

Slab

Materials	kg/m³
Sand 0/4	670
Gravel 2/8	490
Gravel 8/16	790
Cement-CEM I 52.5N	300
Water	150
Superplasticizer BASF MasterGlenium 51	1.67

251

252 Table 4: Mixing procedures for the concrete of both slab and wall

Slab - 5 mins	Wall - 10 mins
Dry mixing for 1 min	Dry mixing for 1 min
Add water while mixing	Add water while mixing
Mixing for 1 min	Mixing for 1 min
Add superplasticizer	Add superplasticizer while mixing and mix for 4 mins
Mixing for 3 mins	Stop at 6 mins and scrape borders for 1 min
	Mixing for 3 mins

253

254 The concrete mixture of the wall was poured into the mould from the top with no vibration since
 255 it was a self-compacting mixture. Three batches were needed to fill the formwork, with the third
 256 batch being mixed 40 minutes after the first one. The pouring of the wall proceeded for 55
 257 minutes and the wall was kept in a climate-controlled room for the whole testing period with a
 258 temperature of $20 \pm 2^\circ\text{C}$ and a relative humidity (RH) of $60 \pm 5\%$. At 19 hours after the contact
 259 between water and cement, the formwork was removed. No curing was applied after formwork
 260 removal. All of the following experiments were additionally performed using these batches
 261 except for the ring test which was performed using a separate batch of concrete.

262 **2.2.2. Testing of fresh concrete properties for the wall**

263 2.2.2.1. Slump flow, density and air content

264 The slump flow was measured according to NBN EN 12350-8 [54]. To determine the density of
265 the fresh self-compacting concrete the method described in NBN EN 12350-6 [56] was followed.
266 The air content of the fresh mixtures was determined using the method described in NBN EN
267 12350-7 [57].

268 2.2.2.2. Final setting time

269 For the final setting time of the mixture, the penetrometer test based on the procedure described
270 in the standard ASTM C 403 [58] was used. This test was used to determine the starting point of
271 the shrinkage measurements.

272 **2.2.3. Hardened concrete properties**

273 2.2.3.1. Compressive strength and E-modulus

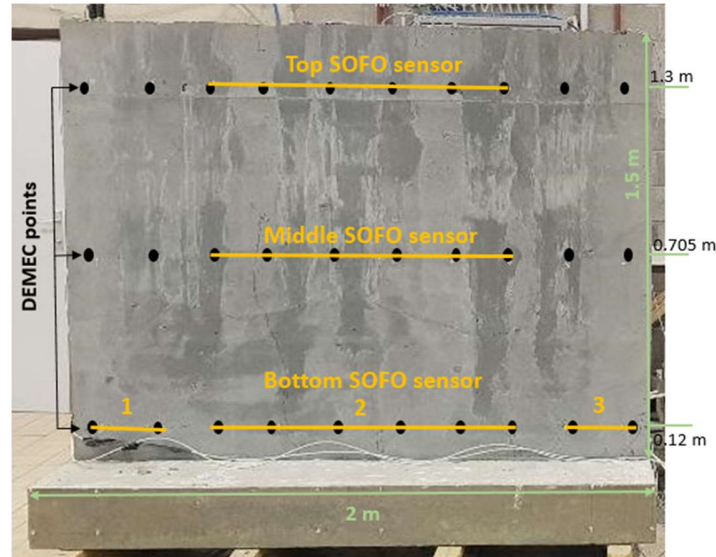
274 The E-modulus and compressive strength tests were determined on triplicate cast cylinders with
275 a height of 300 mm and a diameter of 150 mm according to NBN EN 12390-13 and NBN EN
276 12390-3, respectively [59], [60]. E-modulus and compressive strength were determined at an age
277 of seven days and 85 days for the wall, and 7 and 28 days for the slab.

278 2.2.3.2. Shrinkage

279 Real time deformation behaviour of the wall was measured through fibre optic SOFO sensors
280 (from the company SMARTEC, Switzerland [61]) based on low-coherence interferometry.
281 Sensors were embedded in the wall through attachment to the steel reinforcement mesh before
282 casting. The sensors were mounted at the following three positions: the bottom, the middle and
283 the top annotated respectively as (B), (M) and (T) at a height of 0.120 m, 0.705 m and 1.3 m
284 measured from the slab-wall interface. Five sensors were introduced in the wall, three long
285 sensors with an active length of 1 m (T, M and B2) and two small sensors with an active length
286 of 0.2 m at the bottom edges to monitor AS of the edges: B1 and B3.

287 After demoulding, on the outer surface of the wall, measurement points for demountable
288 mechanical strain gauges (DEMEC) were glued at three levels following the same pattern as the
289 SOFO positions. At the top, middle and bottom, ten measuring points were glued with a 200 mm
290 spacing between the points, and the first and the last point were 100 mm away from the edges.
291 The DEMEC measurements were taken manually each day for 28 days, and then one

292 measurement at 60 days and one at 120 days. The positions of the SOFO sensors and the
293 DEMEC points on the wall can be seen in Figure 2.



294

295 Figure 2: Positions of the embedded fiber optic sensors (SOFO) and the demountable strain
296 gauges points (DEMEC) on the wall

297 Restrained shrinkage

298 Restrained shrinkage was investigated according to the method described in the standard ASTM
299 C 1581-04 [62] known as the ring test method. The deformations of the inner steel ring, which
300 represent the strains of the deforming concrete, were measured at three locations through three
301 strain gauges attached to the ring. Measurements were performed every ten minutes from the
302 time of casting until the age of 20 days. The outer steel ring was removed after 19 hours (same
303 time as formwork removal from the wall), and the rings were sealed with plastic foil to avoid
304 water evaporation, and stored in a climate-controlled room at $20 \pm 2^\circ\text{C}$ and $60 \pm 5\% \text{ RH}$.

305 **3. Results**

306 **3.1. Concrete characterization**

307 **3.1.1. Testing to find the input parameters for the modelling**

308 3.1.1.1. Strength and E-modulus

309 The obtained compressive strengths, direct uniaxial tensile strengths and the E-moduli in tension
310 are the average of three tested specimens, results are presented in

311 Table 5. The tensile E-modulus was found from the load-deformation relation measured in the
 312 uniaxial tensile strength tests, where the E-modulus was deduced as the stress/strain ratio
 313 between 10% and 40% of the failure load.

314 Table 5: Strength and E-modulus of the concrete

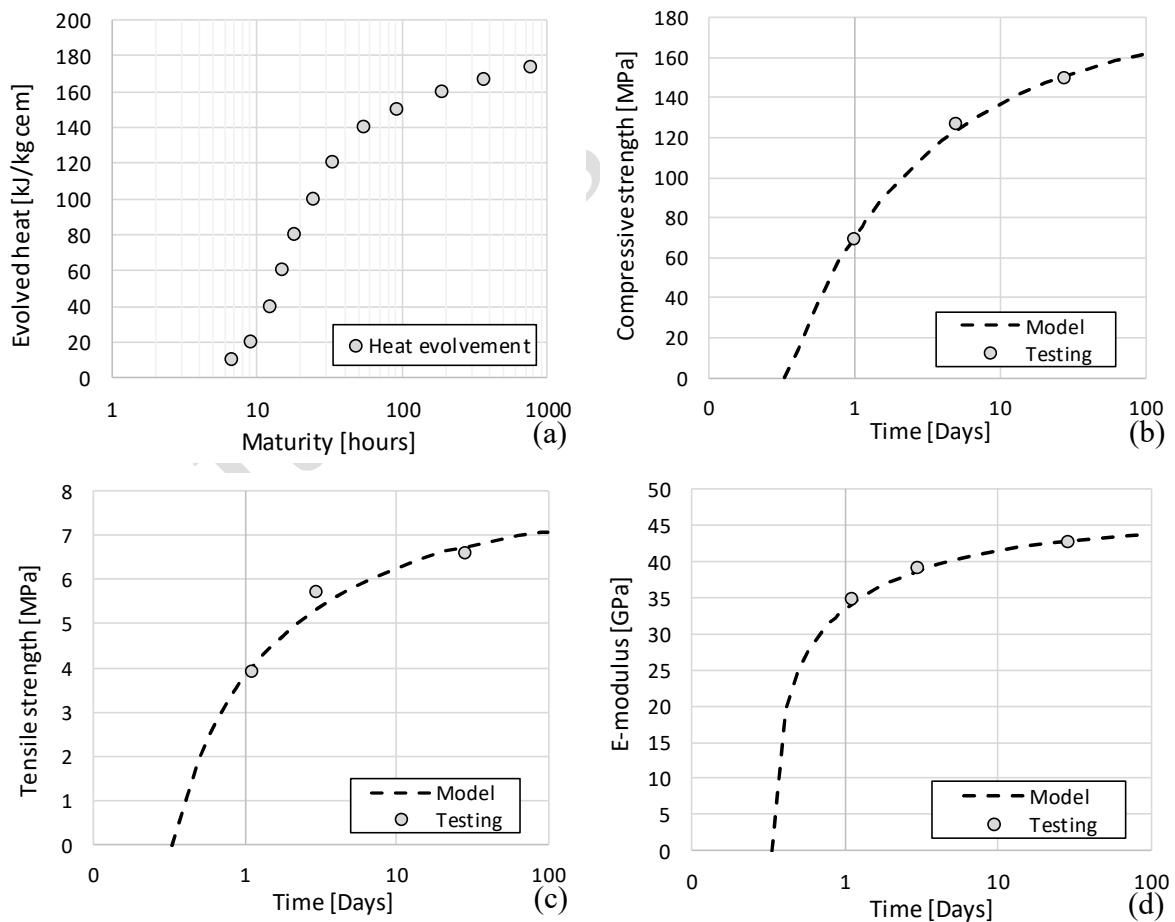
Compressive strength*		Tensile strength**		E-modulus in tension**	
Time [h]	f_c [MPa]	Time [h]	f_t [MPa]	Time [h]	E_c [GPa]
24	68.9	27	3.9	27	34.8
120	126.7	72	5.7	72	39.1
670	149.3	696	6.6	696	42.6

315 * cube strength, 100x100x100 mm³ cubes

316 ** prism strength, 100x100x600 mm³ prisms

317 3.1.1.2. Hydration heat

318 The box was stored in air at 38 °C while the air and concrete temperature were measured
 319 continuously for 4 days. The hydration heat evolution results are presented in Figure 3.



320 Figure 3: Hydration heat evolution (a). Laboratory test results versus model: compressive
321 strength (b), tensile strength (c) and E-modulus (d)

322 **3.1.2. Autogenous shrinkage measured in Free Deformation (FD) and Temperature Stress** 323 **Testing Machine (TSTM)**

324 Autogenous shrinkage was measured up until 289 hours (12 days), and all measurements were
325 zeroed at the starting time for stress development, $t_0 = 8$ hours (found from the TSTM test).
326 Autogenous shrinkage measured in the FD system, i.e. under 20 °C isothermal curing conditions,
327 is provided in Figure 4 (a). The result represents the average measurements of two concrete
328 specimens.

329 The TSTM system is temperature-controlled, the applied temperature history, Figure 4 (b), was
330 determined using the program CTC, and it was based on the calorimetric heat evolution test
331 results and the geometry of a pre-defined wall.

332 The TSTM test was performed in order to determine material- and model parameters for early
333 age crack assessment in CTC. A degree of restraint of only 30% was chosen in order to minimize
334 the restrained stresses during testing, and hence to keep the test running as long as possible to
335 obtain enough data for parameter estimation. The measured stress development of the concrete
336 when subjected to realistic temperature conditions and a degree of restraint of 30% is presented
337 in Figure 4 (b). The specimen developed failure in tension at 4.1 MPa after only 26 hours (51
338 hours of maturity), which is a somewhat lower tensile strength level than found from the
339 corresponding uniaxial tensile strength tests. It should however be noticed that the specimen in
340 the TSTM test was subjected to both realistic temperature conditions and sustained loading prior
341 to failure, i.e. there were considerable variations in the test conditions between the tensile
342 strength test and the TSTM test.

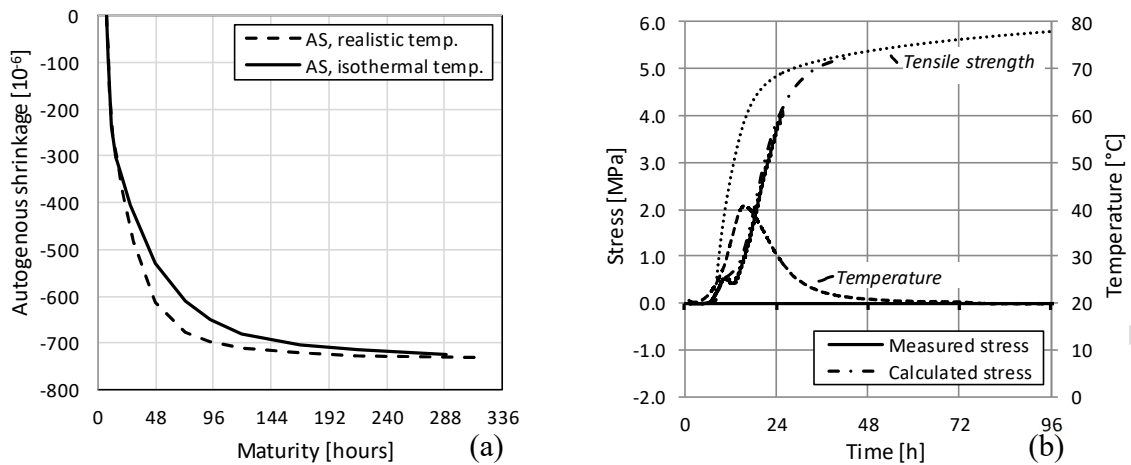
343 In addition to autogenous shrinkage and stress development, tests in the TSTM system also
344 provided the starting time for stress development, t_0 , the incremental E-modulus development
345 and the coefficient of thermal expansion, CTE, for the concrete in question. The starting time for
346 stress development t_0 was found from the restrained stress development test as the maturity time
347 when the measured stress reached 0.1 MPa for tests performed under realistic temperature
348 conditions. After testing, the CTE was determined by applying temperature steps of ± 3 °C
349 around an initial temperature of 20 °C. The CTE was determined as the average value over four

350 such temperature loops. The CTE for the current concrete was found to be $10.7 \times 10^{-6}/^{\circ}\text{C}$ after
351 250 hours of maturity (10 days of maturity).

352 The autogenous shrinkage for the concrete subjected to a realistic temperature history was
353 deduced by subtracting the thermal dilation (calculated by the CTE and the measured
354 temperature) from the total free deformation measured in the dilation rig. The autogenous
355 shrinkage is given in Figure 4 (a), where the curve was zeroed at the starting time for stress
356 development, $t_0 = 8$ hours. The autogenous shrinkage development was observed to be quite
357 similar for both 20°C isothermal and realistic temperature curing conditions, Figure 4 (a).

358 In the current study, the time-dependent behavior of the concrete has been described by
359 viscoelasticity for ageing materials, and more specific, by the double power law [63]. The creep
360 model parameters ϕ_0 , d and p were deduced by the following procedure: The restrained stress
361 development measured in the TSTM was back-calculated by a calculation routine in Excel. The
362 performed stress calculations were based on linear viscoelasticity with age adjusted effects, using
363 the degree of restraint, the measured temperature and free deformation from the dilation rig as
364 input data. The creep parameters were estimated based on previous experience on similar
365 concretes, and then adjusted by fitting the calculated stress development to the measured stress
366 development, Figure 4 (b). The creep model parameters deduced for the current concrete were:
367 $\phi_0 = 0.70$, $d = 0.42$ and $p = 0.26$. The stress development is driven by thermal dilation (TD) and
368 autogenous deformation (AD). Usually, the temperature increase causes an initial compression
369 and appurtenant compressive stress. In the current case, the AD is so high it outcompetes the
370 temperature effect and causes a tensile stress from the start. Between 10 and 12 hours, the AD
371 rate is somewhat lower, and the sum of AD and TD is close to zero. Hence the stress
372 development between 10 and 12 hours is very small due to the lack of volume changes in this
373 period.

374



375 Figure 4: Autogenous shrinkage measured in the FD (isothermal) and the TSTM-system (realistic
 376 temperature evolution), zeroed at t_0 (a); Stress development in the TSTM, realistic curing temperature, R
 377 = 30% (b)

378 3.2. Modelling

379 A model was established in the program CrackTeSt COIN (CTC) [44] in order to simulate the
 380 temperature-, stress- and strength development in the planned UHPC demonstration wall
 381 described in the previous section,

382 Figure 5 (a). The main aim was to assess and predict the cracking risk in the wall, and to
 383 determine further the conditions necessary to achieve cracking at around 20 hours after water
 384 addition. CTC is a two-dimensional special-purpose program for temperature- and stress
 385 calculations in young hardening concrete. A crack risk simulation in CTC comprises a heat flow
 386 analysis followed by a structural analysis. Stress computations in the structural analysis include
 387 stresses in the orthogonal direction according to the boundary conditions given by the user. The
 388 heat and the structural analysis use the same element mesh generated by CTC

389 Figure 5 (b). All in all, CTC provides a crack assessment of a given structure by simulating the
 390 temperature- and stress development, as well as the time and location where the generated stress
 391 exceeds the corresponding tensile strength.

392 The wall geometry was modelled as defined in the previous section, see

393 Figure 5 (a). The ambient temperature and the fresh concrete temperature were assumed to be 23
 394 °C and 20 °C, respectively. The restraint conditions, which vary over the wall height, were
 395 defined by CTC based on the geometry of the structure and the applied concrete. The
 396 investigated concrete was implemented in CTC by a material database file created from the
 397 laboratory test program presented in the previous section. It should be noticed that the program

398 uses autogenous deformation measured in the laboratory versus maturity as input, and does not
399 include the effect of drying. The reason for this is that CTC is generally used for massive
400 structures, where the effect of drying can be neglected. The variation parameters in the currently
401 performed analyses were “type of formwork” as well as “formwork removal time”, which both
402 affect the temperature development, and hence the cracking risk, in the wall. Analyses were run
403 for the wall subjected to three different formwork alternatives:

- 404 ▪ 20 mm plywood removed at 18 hours
- 405 ▪ 20 mm plywood removed at 72 hours
- 406 ▪ 50 mm plywood removed at 72 hours

407 The CTC calculation results are presented in Figure 6, where each graph represents an average
408 value over the hatched area of the wall as illustrated in

409 Figure 5 (a). The hatched area is 50x50 mm² and it is located 150 mm up in the wall when
410 measured from the top of the slab. The restraint is highest close to the underlying foundation,
411 while the temperature increase is highest further up in the wall. The highest stress development is
412 found at the most unfortunate combination of high restraint and high temperature, which for
413 massive walls is considered to be approximately one wall thickness up from the top of the slab
414 [53], [64]. For the current wall, CTC found this location to be at the hatched area illustrated in
415 Figure 5 (a).

416 Simulated temperature developments for the three formwork alternatives are presented in Figure
417 6 (a). The thicker formwork, 50 mm plywood, provided better insulation and hence a higher
418 temperature increase and decrease during curing. For the alternatives with 20 mm plywood, an
419 earlier “formwork removal time” resulted in a somewhat steeper temperature decrease during the
420 cooling period.

421 The simulated stress developments (average over the hatched area) were quite similar over the
422 first 22 hours for all three formwork alternatives, Figure 6 (b). For the given concrete, the early
423 age volume changes are strongly dominated by a very high autogenous deformation (AD).
424 Consequently, a small variation in the curing temperature will only constitute a limited influence
425 on the total early age volume changes, and hence the stress development. The difference in peak
426 temperature between the cases of 50 and 20 mm plywood formwork, is approximately 6 to 7 °C.
427 With a CTE of around $10.7 \times 10^{-6}/^{\circ}\text{C}$, this causes a difference in thermal strain of about 60-70
428 microstrain between the different formworks. The AD at the same time is -420 microstrain. This

429 makes clear that for UHPC, AD is the main driving force for stress development, and a
430 difference of 60-70 microstrains caused by temperature does not have a big influence on the
431 stress development. The increase in tensile strength was slightly higher for the 50 mm plywood
432 alternative due to its higher temperature increase during curing, however, the correspondingly
433 higher temperature-decrease during the cooling phase also caused a somewhat higher stress
434 development over time when compared to the other alternatives, Figure 6 (b). For the wall cast
435 with 20 mm plywood formwork removed at 18 hours after water addition, the generated tensile
436 stress in the hatched area exceeded the corresponding tensile strength at approximately 18 hours
437 after water addition. The cracks will initiate in the wall center, and they have to achieve a certain
438 width to be seen with the naked eye. However, at 20 hours after water addition, it is expected
439 that cracking can be observed for the given demonstration wall.
440

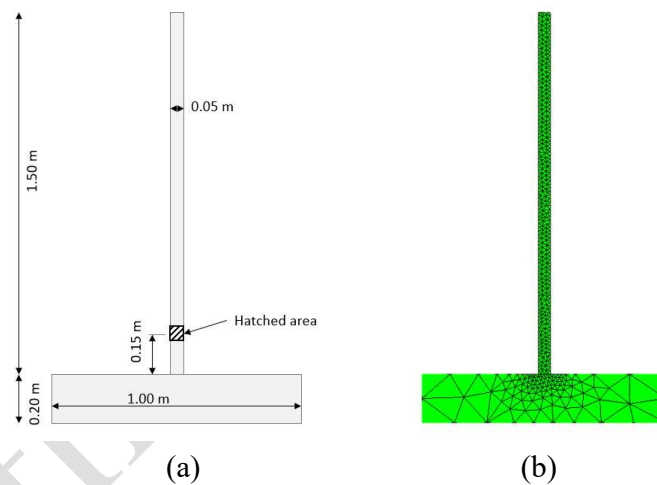


Figure 5: Demonstration wall model for use in CTC (a) and generated mesh (b)

441

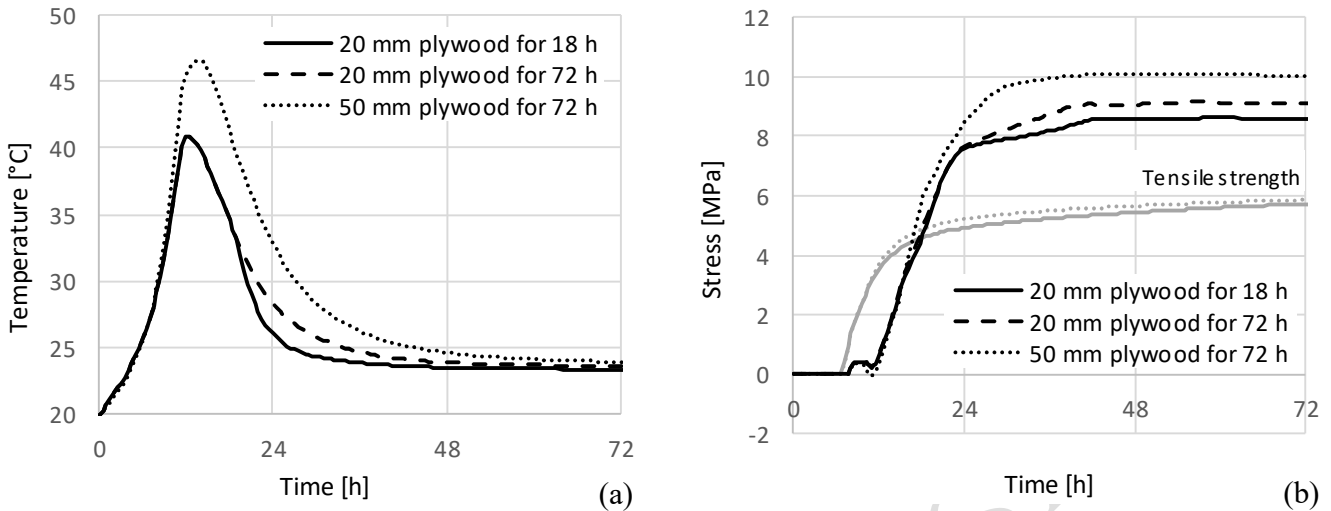


Figure 6: Calculated temperature history (a); Calculated stress- and corresponding strength development (b)

442 3.3. Large-scale demonstrator

443 3.3.1. Fresh concrete properties

444 The slump flow of the wall was equal to 706 ± 22 mm, with an air content of 2.7% and a final
 445 setting time of 5.5 hours. The values represented are the average of the results obtained from the
 446 three batches used for the wall except for the final setting time which was performed only on one
 447 batch.

448 3.3.2. Hardened concrete properties

449 3.3.2.1. Compressive strength and E-modulus

450 The mechanical properties of the concrete used for the demonstration structure (slab + wall) can
 451 be found in Table 6. Note that the measured compressive strength of 87.2 MPa at 7 days of age is
 452 significantly lower than that of the concrete tested for the numerical simulation input (section
 453 2.1.3.2) being 126.7 MPa at 5 d of age. This large difference is confirmed by testing at later ages
 454 too: at 85 d of age the cylinder strength for the demonstration wall was 121 MPa, while the cube
 455 strength of the concrete used for the model input was 149 MPa at 28 days of age. Different
 456 specimen geometry (150/300 mm cylinders vs 100 mm³ cubes), is probably one reason for a
 457 lower value, as it is known that cubes give generally higher measured strength values, in the
 458 order of 5 to 10 percent in UHPC [65]. In addition, several comprehensive studies on high
 459 strength concrete [55], [66], [67] concluded that strength values of 100 mm³ cubes were on
 460 average 11-12 % higher than those of 150/300 mm cylinders. Furthermore, in an old Belgian

461 standard [68], a general formula has been used to estimate with an accuracy of 10% the ratio
 462 between the compressive strength obtained from a 150/300 mm cylinder, R_x , to the compressive
 463 strength obtained from a cube of 100 mm³, R_{w10} . The ratio corresponding to the cylinders used
 464 in this study is $\frac{R_x}{R_{w10}} = 0.75$. Therefore, if we consider the strength value of 121 MPa obtained for
 465 the wall on cylinders, it would correspond to a value of 161 MPa on 100 mm³ cubic specimens,
 466 showing that the differences between cube and cylinder strength can indeed be large.

467 Table 6: Mechanical properties of the concrete used for the demonstration wall (on cylinders, d=150 mm
 468 and h=300 mm)

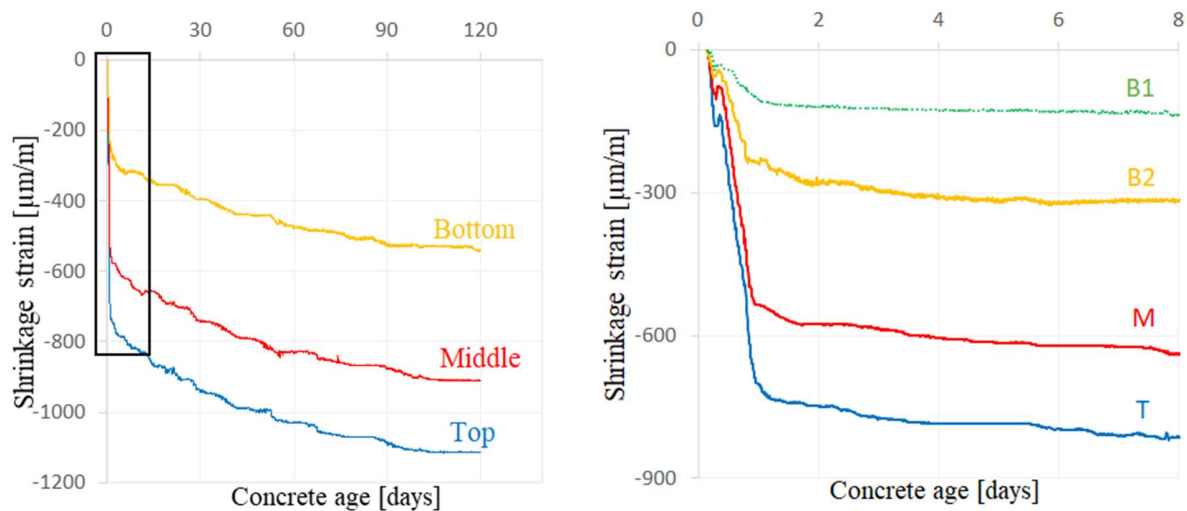
	Compressive strength (MPa) 7 days	E-modulus (GPa) 7 days	Compressive strength (MPa) 28 or 85 days	E-modulus (GPa) 28 or 85 days
Slab	48.8 ± 0.7	-	57.6 ± 2.2 (28 d)	39 ± 8 (28 d)
Wall	87.2 ± 5.7	48	121.1 ± 3.5 (85 d)	47 (85 d)

469

470 3.3.2.2. Shrinkage

471 Measurements of the real-time occurring strains in the wall were obtained automatically from the
 472 fibre optic SOFO sensors embedded inside the wall and are represented in Figure 7. The
 473 measurements were recorded during 4 months to follow the whole period of active shrinkage (as
 474 it can be seen on the shrinkage curves there is no big difference in terms of deformations
 475 between the third and the fourth month), the curves represent the values recorded from the long
 476 sensors with an active length of 1 m. But since the early age cracking risk is discussed in this
 477 study, it is interesting to consider especially the first few days of the concrete age. Thus,
 478 shrinkage values over the first 8 days obtained from the long and one short fiber optic sensor are
 479 represented in Figure 7 on the right. Measurements from the second short sensor (B3 in Figure 2)
 480 could not be presented as there was too much noise in the obtained results. As it can be seen
 481 from the shrinkage curves, the top of the wall shrinks more than the middle and more than the
 482 bottom, demonstrating the influence of the restraining condition at the bottom, i.e. the wall
 483 cannot freely shrink at this location. At around one day, deformation curves transform from a

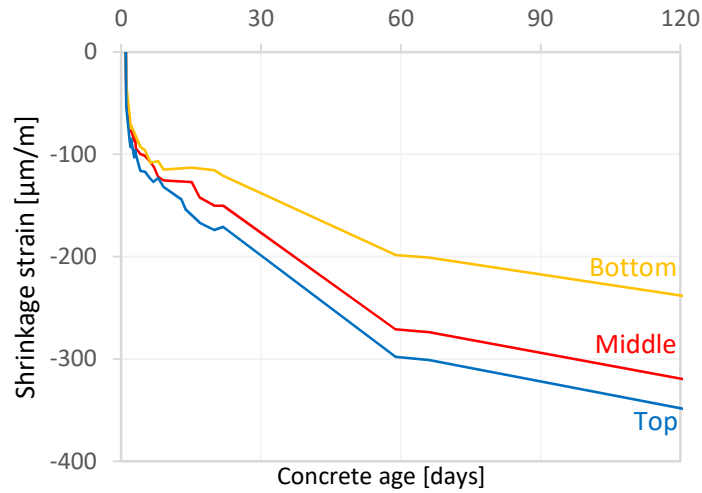
484 very high rate of shrinkage deformations to a much lower shrinkage rate. With water being
 485 rapidly consumed at early age, deformations are expected to increase in low water-to-binder ratio
 486 concrete. After few hours, rigidity of UHPC becomes quickly high which restrains the following
 487 deformations. At the age of 8 days shrinkage values of $-130 \mu\text{m/m}$, $-320 \mu\text{m/m}$, $-640 \mu\text{m/m}$ and $-$
 488 $815 \mu\text{m/m}$ were obtained for bottom 1, bottom 2, middle and top, respectively. At 120 days,
 489 shrinkage values obtained from the long sensors were $-540 \mu\text{m/m}$, $-910 \mu\text{m/m}$ and $-1110 \mu\text{m/m}$
 490 for the bottom, the middle and the top, respectively.



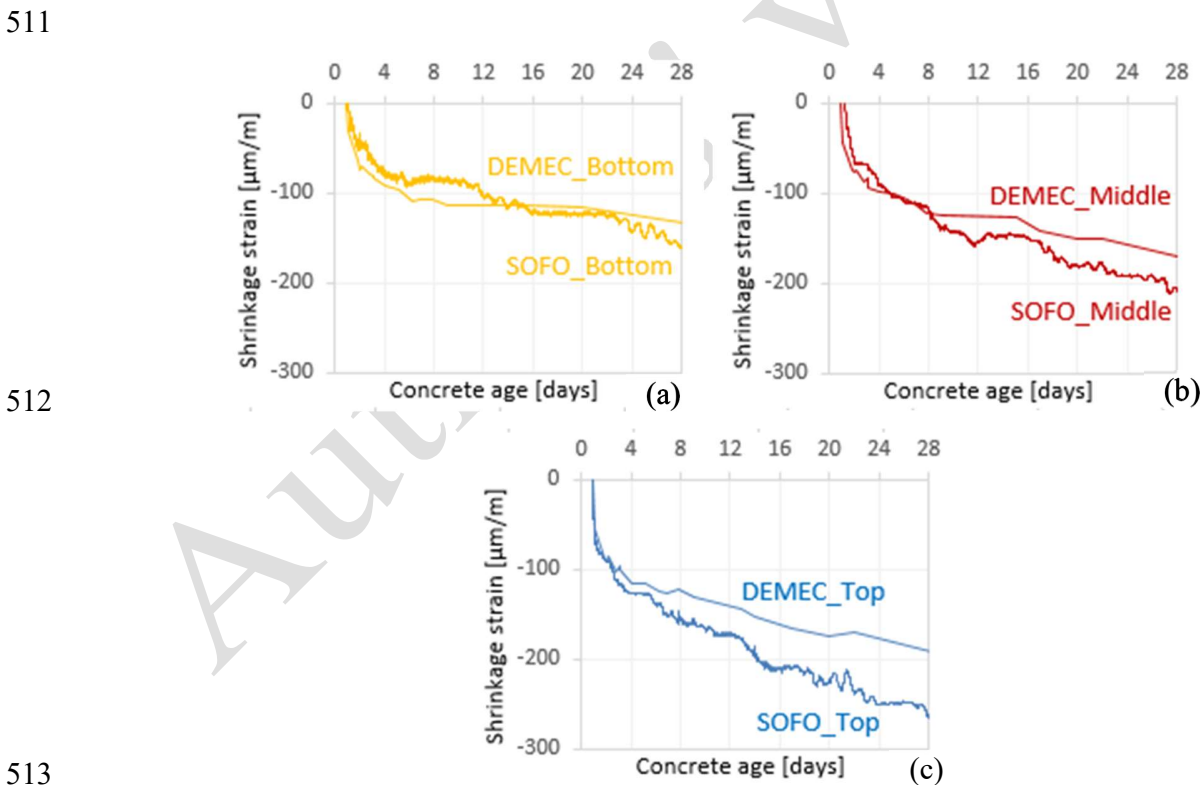
491
 492 Figure 7: Deformations of the top (T), the middle (M) and the bottom (B2) of the wall obtained from the
 493 long fiber optic sensors embedded inside starting from t_0 equal to the final setting time = 5.5 hours for a
 494 period of 4 months (on the left); on the right a zoomed graph over the first 8 days of the deformations in
 495 addition to the deformation curve given by the short sensor B1

496 Shrinkage strain curves obtained from the demountable strain gauges measurements were also in
 497 accordance with the results found from the fiber optic sensors as it can be seen in Figure 8. The
 498 starting point of the DEMEC measurements is taken equal to 23h30 after water-cement contact,
 499 since the points needed to be glued on the wall after formwork removal (the zero point on the
 500 time axis is the contact moment between water and cement). Over the 4 months period of testing,
 501 it was confirmed that the wall has shrunk more at the top than the bottom; a value of $360 \mu\text{m/m}$
 502 is reached for the top, $330 \mu\text{m/m}$ for the middle and $250 \mu\text{m/m}$ for the bottom. In Figure 9 the
 503 results from the SOFO measurements are compared with the ones obtained from the DEMEC
 504 measurements over the first 28 days, during which regular DEMEC measurements were taken.
 505 The curves were plotted from an age of 23h30 after water-cement contact (the time where the

506 first DEMEC measurements were obtained), and the two sensor types followed the same
 507 behavior over 28 days.



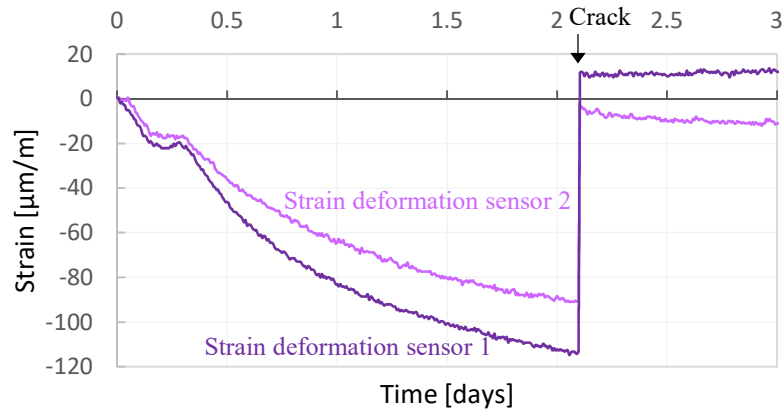
508
 509 Figure 8: Deformation measurements obtained from the demountable strain gauges (DEMEC) starting at
 510 an age of 23.5h after water-cement contact



513
 514 Figure 9: Comparison of the occurring shrinkage strain results obtained from the fiber optic SOFO sensors
 515 and the demountable strain gauges (DEMEC), starting at an age of 23.5h after water-cement contact (a) is
 516 for the bottom, (b) for the middle and (c) for the top positions on the wall

517 Restrained shrinkage

518 The results of the restrained shrinkage test are presented in Figure 10, each curve represents the
519 values obtained from the sensors attached to the ring (one sensor was not working properly
520 therefore only two out of three are shown). Time zero is equalled to the water-cement contact
521 and the curves are plotted from the age of one hour. The sudden jump in the curve represents the
522 time of cracking, where the sensors measure an abrupt change. The strain values reached about -
523 100 $\mu\text{m}/\text{m}$ before the sample cracked at around 2 days.



524

525 Figure 10: Restrained shrinkage results obtained from the ring method; the zero point on the time axis
526 represents the moment of water-cement contact

527 4. Discussion

528 4.1. Comparison of stress development and time of cracking

529 The work comprises three different approaches to determine stress development and subsequent
530 cracking assessment:

- 531 a) TSTM test with 30% restraint
- 532 b) Numerical simulation of the wall
- 533 c) Strain measurements and visual observation of the wall

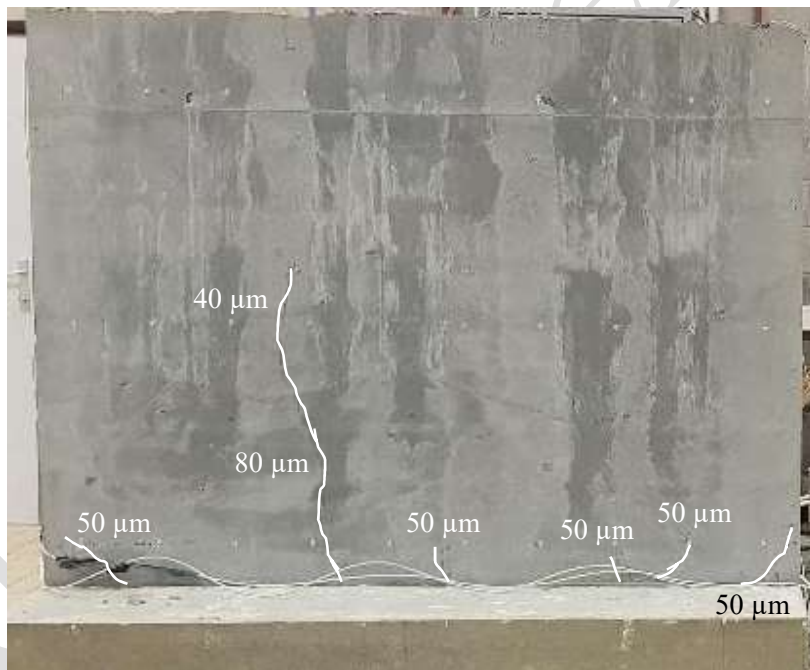
534

535 The TSTM test measured the stress development in the hardening phase for a specimen subjected
536 to a degree of restraint of 30%. This restraint did not represent the given demonstration wall, but
537 it was applied in order to minimize the restrained stress during testing, i.e. to keep the test
538 running as long as possible to obtain enough data for parameter estimation. Despite the low
539 restraint, the TSTM specimen developed failure in tension as early as 26 hours after water
540 addition, confirming that the investigated concrete is very prone to early age cracking.

541 The degree of restraint in a wall varies over the wall height and length, and it depends on several
542 parameters: the area, the geometry and the stiffness of both the wall and the base slab, the elastic
543 properties of the ground beneath, the length to height ratio of the wall, as well as possible slip
544 failures between the wall and the base slab. The wall deformation measurements in Figure 7 and
545 illustrate how the restraint in the wall decreases with increasing distance from the joint, i.e.
546 increasing deformations with increasing distance from the base slab; this represents the very
547 typical relation between restraint and the distance from the base as reported by Schlee [69],
548 **Erreur ! Source du renvoi introuvable.** where several tests were conducted on micro-concrete
549 walls with different length-to-height ratios cast on a steel slab. For a wall cast on a massive
550 concrete base it is suggested by BS 8110 2 [70] that the restraint factor at the joint lies between
551 0.6 and 0.8. This corresponds well with a simplified calculation method presented by CIRIA
552 C766 [33], which estimated the given wall to have a degree of restraint at the joint of 0.78, i.e.
553 78%. The same calculation estimated a degree of restraint of 30% to occur approx. 550 mm
554 above the joint. In the TSTM test, the specimen reached a tensile stress of 4.1 MPa after 26
555 hours, Figure 5. Correspondingly, the CTC simulations showed a restrained stress of approx. 4.8
556 MPa after 26 hours in an area 550 mm above the joint. Although these approaches were not fully
557 comparable due to variations in their temperature histories as well as the restraint considerations
558 discussed in the following section, they did provide restrained stresses in the same order of
559 magnitude, indicating rather good agreement.

560 The first crack in the demonstration wall was reported two hours after formwork removal (21
561 hours after water-cement contact). This was a through-going crack that reached the middle height
562 of the wall, followed by other non through-going cracks (except at the edges) as depicted in
563 Figure 11. The CTC stress simulation estimated the generated tensile stress in the critical part of
564 the wall to exceed the corresponding tensile strength somewhat earlier, at approx. 18 hours after
565 water addition. However, the given demonstration wall has a low length to height ratio $L/H = 1.3$
566 < 3 , meaning that the Bernoulli-Euler assumption of “plane sections remain plane when
567 deforming” cannot be applied. This may cause 3D effects in terms of a reduction of restraint and
568 hence stresses in the wall, and these effects may not be captured by the two-dimensional CTC
569 simulation. Consequently, due to the low length to height ratio of the wall, the CTC simulation
570 was expected to provide a somewhat higher restraint and stress development than the actual wall.
571 In addition, the demonstration wall seemed to experience some slip failure between the wall and

572 the base slab, Figure 11, which also reduces the degree of restraint. Summarized, the degree of
573 restraint in the demonstration wall was expected to be somewhat lower than the degree of
574 restraint determined by CTC in the simulations, i.e. the stress development and cracking of the
575 wall was expected to occur somewhat later than estimated by the simulation. The program CTC,
576 which is intended for massive concrete structures, does not include the effect of drying. Drying
577 shrinkage is generally not considered to have a big influence on UHPC/HPC structures, and in
578 addition, the analysis expects the first crack to appear at approx. 18 hours after water addition,
579 which is the same time as formwork removal. Before 18 hours, the formwork will prevent
580 drying, and hence the possible drying-induced inaccuracy of the simulation prior to the first
581 crack can be neglected. All things considered, the simulated stress development and crack
582 assessment showed good agreement with the observations of the demonstration wall.
583



584
585 Figure 11: Crack development on the wall with the approximated crack width at each position

586 In addition, regarding the ring test, the observed jumps in Figure 10 represent cracking of the
587 rings that took place at around 2 days after water-cement contact, a cracking time that was later
588 than that for the wall. The main reason is the huge difference in the experimental set-up between
589 the ring and the wall, e.g. the geometries and restraining conditions, that highly influence the

590 induced stresses. In addition, the wall also experienced larger additional thermal contraction
591 following the hydration heat peak.

592 **4.2. Shrinkage measurements**

593 The work comprises four different deformation measurements:

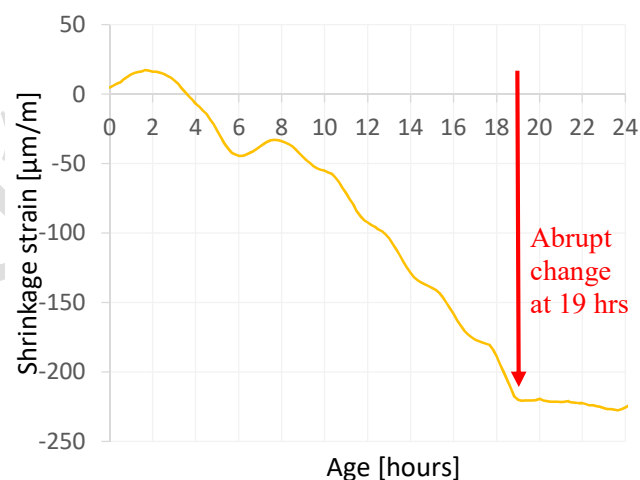
- 594 a) Free deformation measured in the FD-system (isothermal)
- 595 b) Free deformation measured in the TSTM-system (realistic temperature)
- 596 c) Shrinkage strains occurring in the wall under various restraint conditions, measured with
597 two different systems (realistic temperature)
- 598 d) Restrained shrinkage deformations measured in the ring test (isothermal)

599

600 AS was measured under 20 °C isothermal conditions in the FD-system, and under realistic
601 temperature conditions in the TSTM-system. Both measurements were zeroed at the starting time
602 for stress development, $t_0 = 8$ hours, as determined from the TSTM test. The AS development
603 was observed to be quite similar for both 20 °C isothermal and realistic temperature curing
604 conditions, Figure 4 (a), as opposed to other concretes where realistic curing temperature regimes
605 have been found to initiate fundamental differences in the AS development when compared to 20
606 °C isothermal curing [71]. The free deformation measurements in the TSTM-system include both
607 autogenous deformation and thermal dilation. The demonstration wall was rather thin, with a
608 thickness of only 50 mm, however, due to the high cement content and corresponding heat
609 evolvment, the given wall experienced a temperature increase of as much as 20 °C during
610 curing. This caused a thermal expansion and contraction of about 200 microstrains, which still
611 was far less than the deduced AS which reached a level of 700 microstrains after approximately
612 one week. It is thus evident that the considerable amount of AS found for the investigated
613 concrete constitutes the main mechanism when it comes to early age volume changes and hence
614 the cracking risk of the demonstration wall.

615 Under surrounding temperature ($20 \pm 2^\circ\text{C}$ and $60 \pm 5\%$ RH), real-time deformations of the wall
616 were measured automatically by the fiber optic SOFO sensors and manually by the demountable
617 DEMEC strain gauges. In Figure 7, results obtained from the SOFOs are plotted where the
618 influence of the restraining condition at the bottom is clearly shown. The wall undergoes a lot of
619 shrinkage strains at the top where it is more free to shrink with less stresses. Then, these strains
620 gradually decrease when approaching the restraining condition at the bottom near the slab-wall

621 connection. On the left of Figure 7, a big difference is seen between the shrinkage values of the
 622 bottom sensor and the middle/top sensors, as the shrinkage strain difference between the top and
 623 the middle is around 200 $\mu\text{m}/\text{m}$ whereas the one between the middle and the bottom is around
 624 400 $\mu\text{m}/\text{m}$. The behavior of the bottom curve was studied at the very early age (0-24h) as seen in
 625 Figure 12, and a change of the slope of the shrinkage strain curve was seen at around 19 hours
 626 which equals to 21 hours after water-cement contact (taking into account a gap of 2 hours that
 627 represents the time to cast the wall and to put the sensors into operation). The abrupt change in
 628 Figure 12 represents the formation of the cracks, which was seen with the naked eye 2 hours after
 629 formwork removal (formwork was removed at 19 hours after water-cement contact). The longest
 630 and first crack passed through the bottom sensor, for that reason there was a relaxation of the
 631 stresses at that location which explains the big difference between the bottom and the middle-top
 632 strain curves. At the final measurement (120 days after casting of the wall) this crack had a
 633 length of 850 mm and a width of 180 μm at the bottom of the wall. Halfway the crack height the
 634 width was 80 μm and at the top of the crack the width was 40 μm . Using the same interpretation,
 635 the shrinkage values of the bottom sensor B1 near the edge of the wall were 23% lower than for
 636 the long bottom sensor 2 in the middle, due to the presence of many cracks that were clearly
 637 apparent at the edges of the wall. Since B1 had more cracks over its smaller length, it measured
 638 less strain deformations than B2.



639
 640 Figure 12: Representation of the shrinkage measurements obtained from the long bottom fiber optic
 641 sensor embedded inside of the wall at the early age (24 h)

642 Shrinkage strains of the wall were also manually measured with demountable strain gauges.
 643 Values are shown in Figure 8 over a period of 4 months (same as for the SOFOs). These curves

644 follow the same trend as the SOFOs and also show the influence of the restraining condition at
645 the bottom. The ranges of the DEMEC values at the end of the testing period are lower than the
646 ranges of strains of the SOFOs (Figure 7), which is due to the difference in the starting point of
647 the measurements. For the DEMEC measurements, points need to be glued on the wall after
648 formwork removal and first measurements are taken after the glue dried which was roughly
649 around 3.5 hours after formwork removal. Therefore, measurements started after 23.5 hours
650 when a big part of the occurring strains had already happened. A comparison between the SOFO
651 and DEMEC measurements for the first 28 days of age was performed in Figure 9. The starting
652 point of the measurements in this figure was taken to be 23.5 hours after water-cement contact
653 for both techniques. The SOFO measurements showed slightly higher strain values at the
654 different levels. Drying shrinkage is normally not considered to have a big influence on
655 UHPC/HPC structures. Zhang et al. found that most of the total shrinkage undergone by high
656 strength concrete (containing silica fume) could be attributed to AS rather than drying shrinkage
657 due to the dense and impermeable matrix [72]. Xie et al. performed autogenous and free total
658 shrinkage on UHPC prisms and showed that drying shrinkage comprises approximately 20% of
659 the total measured shrinkage. In addition, during early concrete ages (until 7 days after water to
660 cement contact), drying shrinkage is not considered since the difference between the free total
661 and autogenous shrinkage curves is negligible [73]. Nevertheless, water evaporation near the
662 surface of the wall could have been faster than deeper inside the matrix, which could have led to
663 a slightly lower level of cement hydration and therefore slightly lower shrinkage strains obtained
664 from DEMEC measurements. In addition, the rapid water evaporation at the surface will enhance
665 the formation of microcracks which leads to a relaxation of stresses around the crack itself. This
666 also justifies the lower DEMEC shrinkage strain curves.

667 The ring test method was used to evaluate the shrinkage under restrained conditions. As it can be
668 seen in Figure 10, samples reached a strain of $-120 \mu\text{m}/\text{m}$ before cracking after 2 days. Under
669 realistic temperature and RH conditions ($20 \pm 2^\circ\text{C}$ and $60 \pm 5\% \text{RH}$), the wall cracked two hours
670 after formwork removal at around 21 hours after water-cement contact while rings cracked at a
671 later age. This could be justified by the fact that the wall experienced larger additional thermal
672 contraction following the hydration heat peak in addition to the differences in geometry and
673 restraining conditions existing between the wall and the ring.

674 **5. Conclusion**

675 To predict the risks of early age shrinkage cracking for UHPC, a numerical model, which has
676 been established primarily for normal concrete, has been further developed and applied on a
677 demonstration wall with high risk of cracking, cast on a non-deforming slab. Thus, an early age
678 crack assessment was performed in this study using a numerical simulation model applied on a
679 typical restrained wall. A demonstration structure (a wall cast on a non-deforming slab) has then
680 been built in order to verify the simulated cracking risk through visual observation of cracking
681 and deformation measurements of the wall. A comparison between the numerical simulation
682 results and the actual measurements was presented. The currently used UHPC showed a
683 considerable autogenous shrinkage, constituting the main driving mechanism to the early age
684 volume changes and the corresponding high cracking risk of the investigated wall.

685 The following conclusions can be drawn:

686

- 687 • The comparison between the numerical simulation results and the actual measurements
688 proved that the proposed model is suitable for UHPC-concrete. A good fit between the
689 model and experimental results was found for the development of compressive strength,
690 tensile strength and E-modulus in tension. In addition, the performed tests and analyses
691 confirmed that UHPCs are very prone to early age cracking due to the high AS
692 development as well as the high temperatures generated during curing even though the
693 wall was rather thin. Indeed, the model highlighted the increased risk of cracking due to
694 the increased degree of restraint associated with the small wall thickness.
- 695 • The numerical simulation gave a good prediction of the cracking risk in the wall:
696 cracking was predicted to appear at approximately 20 hours after water addition, and the
697 first crack was observed in the wall at 21 hours after contact between cement and water.
698 Hence, the novelty of the model remains in the time prediction of crack development
699 rather than the crack development itself. The through-going crack observed in the
700 demonstration wall reached the mid height of the wall with a width of 180 μm at its
701 bottom, 80 μm at its middle and 40 μm at its top. The crack was followed by other
702 similar small cracks with a width of 50 μm .
- 703 • Autogenous shrinkage results under isothermal and realistic conditions followed the same
704 behavior and experimental and modelled results were in the same range. Under realistic

705 conditions the occurring strains in the wall were recorded automatically using fiber optic
706 sensors embedded inside the wall and manually with demountable strain gauges through
707 points glued on the outer surface of the wall. Another key point to stress on, AS
708 deformations can be measured in different ways for big/massive structures where it was
709 shown that AS is very dependent on the zeroing time of measurements as well.

- 710 • Restrained shrinkage tests were performed on the cast concrete using the ring test
711 method. Rings cracked at 2 days, a later time than the wall, which is probably because the
712 wall experienced larger additional thermal contraction following the hydration heat peak
713 in addition to the effect of a difference in geometry and restraining conditions that exists
714 between the ring and the wall.

715 **Acknowledgement**

716 These results are part of a project that has received funding from the European Union's Horizon
717 2020 research and innovation programme under grant agreement N°685445 – LORCENIS and
718 from the Research Foundation Flanders (FWO Vlaanderen) under project No G.0A28.16. The
719 authors gratefully acknowledge the support and provision of materials from Dirk Qvaeschning
720 and Sara Irico (Dyckerhoff GmbH). The data that support the findings of this study are available
721 from the corresponding author upon reasonable request.

722

723 **6. References**

- 724 [1] D. P. Bentz, O. M. Jensen, K. K. Hansen, J. F. Olesen, H. Stang, and C. J. Haecker,
725 “Influence of Cement Particle-Size Distribution on Early Age Autogenous Strains and
726 Stresses in Cement-Based Materials,” *J. Am. Ceram. Soc.*, vol. 84, no. 1, pp. 129–135,
727 2001, doi: 10.1111/j.1151-2916.2001.tb00619.x.
- 728 [2] V. Baroghel-bouny *et al.*, “Autogenous Deformations of Cement Pastes : Part II . W/C
729 effects , Micro-Macro Correlations , and Threshold values,” 2006.
- 730 [3] L. Wu, N. Farzadnia, C. Shi, Z. Zhang, and H. Wang, “Autogenous shrinkage of high
731 performance concrete: A review,” *Construction and Building Materials*, vol. 149. 2017,
732 doi: 10.1016/j.conbuildmat.2017.05.064.
- 733 [4] A. Loukili, A. Khelidj, and P. Richard, “Hydration kinetics, change of relative humidity,
734 and autogenous shrinkage of ultra-high-strength concrete,” *Cem. Concr. Res.*, vol. 29, no.
735 4, pp. 577–584, 1999, doi: 10.1016/S0008-8846(99)00022-8.
- 736 [5] V. Mechtcherine and H.-W. Reinhardt, *Application of Superabsorbent Polymers (SAP) in*
737 *Concrete Construction*. 2012.
- 738 [6] L. De Meyst, J. Kheir, J. R. Tenório Filho, K. Van Tittelboom, and N. De Belie, “The use
739 of superabsorbent polymers in high performance concrete to mitigate autogenous

- 740 shrinkage in a large-scale demonstrator,” *Sustain.*, vol. 12, no. 11, 2020, doi:
741 10.3390/su12114741.
- 742 [7] P. Lura, K. Van Breugel, and I. Maruyama, “Effect of curing temperature and type of
743 cement on early-age shrinkage of high-performance concrete,” *Cem. Concr. Res.*, vol. 31,
744 pp. 1867–1872, 2001.
- 745 [8] A. Darquennes, S. Staquet, and B. Espion, “Determination of time-zero and its effect on
746 autogenous deformation evolution,” *Eur. J. Environ. Civ. Eng.*, vol. 15, no. 7, pp. 1017–
747 1029, 2011, doi: 10.1080/19648189.2011.9695290.
- 748 [9] Z. Hu *et al.*, “A review on testing methods for autogenous shrinkage measurement of
749 cement-based materials,” *J. Sustain. Cem. Mater.*, vol. 2, no. 2, pp. 161–171, 2013, doi:
750 10.1080/21650373.2013.797937.
- 751 [10] A. Loukili *et al.*, “A New Approach to Determine Autogenous Shrinkage of Mortar at
752 Early Age Considering Temperature History,” *Cem. Concr. Res.*, pp. 0–8, 2017.
- 753 [11] E.-I. Tazawa and S. Miyazawa, “Influence of cement and admixture on autogenous
754 shrinkage of cement paste,” *Cem. Concr. Res.*, vol. 25, no. 2, pp. 281–287, 1995.
- 755 [12] O. Mejlhede Jensen and P. Freiesleben Hansen, “A dilatometer for measuring autogenous
756 deformation in hardening portland cement paste,” *Mater. Struct.*, vol. 28, no. 7, pp. 406–
757 409, 1995, doi: 10.1007/BF02473076.
- 758 [13] E. Tazawa and S. Miyazawa, “Effect of constituents and curing condition on autogenous
759 shrinkage of concrete,” in *Autogenous Shrinkage of Concrete*, London: E & FN Spon,
760 1999, pp. 267–280.
- 761 [14] H. K. Lee, K. M. Lee, and B. G. Kim, “Autogenous shrinkage of high-performance
762 concrete containing fly ash,” *Mag. Concr. Res.*, vol. 55, no. 6, pp. 507–515, 2003, doi:
763 10.1680/macr.2003.55.6.507.
- 764 [15] Y. Li and J. Li, “Capillary tension theory for prediction of early autogenous shrinkage of
765 self-consolidating concrete,” *Constr. Build. Mater.*, vol. 53, pp. 511–516, 2014, doi:
766 10.1016/j.conbuildmat.2013.12.010.
- 767 [16] R. Wendner, M. H. Hubler, and Z. P. Bažant, “The B4 model for multi-decade creep and
768 shrinkage prediction,” *Mech. Phys. Creep, Shrinkage, Durab. Concrete A Tribut. to Zdenek*
769 *P. Bazant - Proc. 9th Int. Conf. Creep, Shrinkage, Durab. Mech. CONCREEP 2013*, no.
770 September 2013, pp. 429–436, 2013, doi: 10.1061/9780784413111.051.
- 771 [17] Z. P. Bažant and S. Baweja, “Justification and refinements of model B3 for concrete creep
772 and shrinkage 1. statistics and sensitivity,” *Mater. Struct.*, vol. 28, no. 7, pp. 415–430,
773 1995, doi: 10.1007/BF02473078.
- 774 [18] F. Benboudjema *et al.*, “COST TU1404 benchmark on macroscopic modelling of concrete
775 and concrete structures at early age: Proof-of-concept stage,” *Constr. Build. Mater.*, vol.
776 174, pp. 173–189, 2018.
- 777 [19] J. Walraven and A. Bigaj-van Vliet, *fib Model Code for Concrete Structures 2010*, no.
778 October. 2013.
- 779 [20] D. Bosnjak, “Self-induced Cracking Problems in Hardening Concrete Structures,”
780 Norwegian University of Science and Technology, 2000.
- 781 [21] S. Altoubat A and D. Lange, “Creep, Shrinkage, and Cracking of Restrained Concrete at
782 Early Age,” *Mater. J.*, vol. 98, no. 4, pp. 323–331, 2001.
- 783 [22] D. S. Atrushi, “Tensile and Compressive Creep of Early Age Concrete: Testing and
784 Modelling,” Norwegian University of Science and Technology, 2003.
- 785 [23] G. De Schutter, “Applicability of degree of hydration concept and maturity method for

- 786 thermo-visco-elastic behaviour of early age concrete,” *Cem. Concr. Compos.*, vol. 26, no.
787 5, pp. 437–443, 2004, doi: 10.1016/S0958-9465(03)00067-2.
- 788 [24] F. Benboudjema and J. M. Torrenti, “Early-age behaviour of concrete nuclear
789 containments,” *Nucl. Eng. Des.*, vol. 238, no. 10, pp. 2495–2506, 2008, doi:
790 10.1016/j.nucengdes.2008.04.009.
- 791 [25] D. Schlicke and N. V. Tue, “Consideration of Viscoelasticity in Time Step FEM-Based
792 Restraint Analyses of Hardening Concrete,” *J. Mod. Phys.*, vol. 04, no. 10, pp. 9–14,
793 2013, doi: 10.4236/jmp.2013.410a2002.
- 794 [26] R. Springenschmid, “Prevention of Thermal Cracking in Concrete at Early Ages -
795 Preface,” London, Great Britain, 1998. doi: ISBN 9780367447670.
- 796 [27] G. De Schutter, “Fundamental study of early age concrete behaviour as a basis for durable
797 concrete structures,” *Mater. Struct.*, vol. 35, no. 245, pp. 15–21, 2002.
- 798 [28] F. Czerny, K. Van Breugel, and E. A. B. Koenders, “The reliability of crack predictions
799 for hardening concrete structures,” in *Proceedings of the International Conference on
800 Cement Combinations for Durable Concrete*, 2005, pp. 757–766, doi:
801 10.1680/ccfdc.34013.0083.
- 802 [29] J. Guomin, “Cracking Risk of Concrete Structures in The Hardening Phase,” Norwegian
803 University of Science and Technology (NTNU), 2008.
- 804 [30] I. Pane and W. Hansen, “Predictions and verifications of early-age stress development in
805 hydrating blended cement concrete,” *Cem. Concr. Res.*, vol. 38, no. 11, pp. 1315–1324,
806 2008, doi: 10.1016/j.cemconres.2008.05.001.
- 807 [31] F. Barre *et al.*, *Control of Cracking in Reinforced Concrete Structures: Research project
808 CEOS.fr*. France, 2016.
- 809 [32] A. B. E. Klausen, “Early age crack assessment Codes , guidelines and calculation methods
810 D. WP1.2 (Ed.) DaCS Project Report No 2,” Trondheim, Norway, 2018.
- 811 [33] P. Bamforth, *Control of cracking caused by restrained deformation in concrete (C766)*.
812 CIRIA, 2018.
- 813 [34] R. Lackner and H. A. Mang, “Chemoplastic material model for the simulation of early-age
814 cracking: From the constitutive law to numerical analyses of massive concrete structures,”
815 *Cem. Concr. Compos.*, vol. 26, no. 5, pp. 551–562, 2004, doi: 10.1016/S0958-
816 9465(03)00071-4.
- 817 [35] M. Cervera, J. Oliver, and T. Prato, “Thermo-Chemo-Mechanical Model For Concrete. II:
818 Damage and Creep,” *J. Eng. Mech.*, no. September, pp. 1028–1039, 1999, doi:
819 http10.1061/(ASCE)0733-9399(1999)125:9(1028).
- 820 [36] D. Gawin, F. Pesavento, and B. A. Schrefler, “Hygro-thermo-chemo-mechanical
821 modelling of concrete at early ages and beyond. Part II: Shrinkage and creep of concrete,”
822 *Int. J. Numer. Methods Eng.*, vol. 67, no. 3, pp. 332–363, 2006, doi: 10.1002/nme.1636.
- 823 [37] G. P. A. G. van Zijl, R. de Borst, and J. G. Rots, “A numerical model for the time-
824 dependent cracking of cementitious materials,” *Int. J. Numer. Methods Eng.*, vol. 52, no.
825 7, pp. 637–654, 2001, doi: 10.1002/nme.211.
- 826 [38] P. Morabito, “Methods to Determine the Heat of Hydration of Concrete,” in *Prevention of
827 Thermal Cracking in Concrete at Early Ages*, R. Springenschmid, Ed. Munich, Germany:
828 CRC Press, 1998.
- 829 [39] O. M. Jensen and P. F. Hansen, “Influence of temperature on autogenous deformation and
830 relative humidity change in hardening cement paste,” *Cem. Concr. Res.*, vol. 29, no. 4, pp.
831 567–575, 1999, doi: 10.1016/S0008-8846(99)00021-6.

- 832 [40] Z. P. Bažant, “Prediction of concrete creep and shrinkage: Past, present and future,” *Nucl.*
833 *Eng. Des.*, vol. 203, no. 1, pp. 27–38, 2001, doi: 10.1016/S0029-5493(00)00299-5.
- 834 [41] T. Kanstad, T. A. Hammer, Ø. Bjøntegaard, and E. J. Sellevold, “Mechanical properties of
835 early age concrete: Evaluation of test methods for tensile strength and modulus of
836 elasticity. Determination of model parameters. IPACS report,” Sweden, 2001.
- 837 [42] M. Nilsson, “Restraint Factors and Partial Coefficients for Crack Risk Analyses of Early
838 Age Concrete Structures,” Luleå University of Technology, Sweden, 2003.
- 839 [43] A. E. Klausen, T. Kanstad, and Ø. Bjøntegaard, “Hardening Concrete Exposed to Realistic
840 Curing Temperature Regimes and Restraint Conditions: Advanced Testing and Design
841 Methodology,” *Adv. Mater. Sci. Eng.*, vol. 2019, p. 15, 2019, doi: 10.1155/2019/9071034.
- 842 [44] “JEJMS Concrete AB, CrackTeSt COIN (2009-2012).” Luleå, Sweden.
- 843 [45] “COIN: Concrete Innovation Centre - a centre for research based innovation.,” *Research*
844 *Council of Norway*, 2007. <https://www.sintef.no/en/projects/coin/coinp> (accessed Sep. 23,
845 2019).
- 846 [46] “Sustainable Building with Ultra-High Performance Concrete. Main report from the
847 German Priority Program 1182 of the German Research Foundation: Heft 22 Structural
848 Materials and Engineering Series, UNI Kassel, Germany Ed.: M. Schmidt et al., 2014.,”
849 Kassel, Germany, 2014.
- 850 [47] L. De Meyst, J. Kheir, J. R. Tenório Filho, K. Van Tittelboom, and N. De Belie, “The use
851 of superabsorbent polymers in high performance concrete to mitigate autogenous
852 shrinkage in a large-scale demonstrator,” *Sustain.*, vol. 12, no. 11, 2020, doi:
853 10.3390/su12114741.
- 854 [48] “NS-EN 12390-3, Testing hardened concrete - Part 3: Compressive strength of test
855 specimens, Standard Norge, Norway,” 2009.
- 856 [49] Instron, “INSTRON 5980 Series, Norwood, MA, USA,” 2019. .
- 857 [50] Ø. Bjøntegaard, “Thermal Dilation and Autogenous Deformation as Driving Forces to
858 Self-Induced Stresses in High Performance Concrete,” Norwegian University of Science
859 and Technology (NTNU), Trondheim, Norway, 1999.
- 860 [51] “CEB-FIP Model Code 1990: Design code, Comité Euro-International du Béton,
861 0727716964, 9780727716965, Lausanne, Switzerland,” 1991.
- 862 [52] T. Kanstad, T. A. Hammer, Ø. Bjøntegaard, and E. J. Sellevold, “Mechanical properties of
863 young concrete: Part II: Determination of model parameters and test program proposals,”
864 *Mater. Struct.*, vol. 36, no. 4, pp. 226–230, 2003, doi: 10.1007/bf02479615.
- 865 [53] Ø. Bjøntegaard, “Basis for and practical approaches to stress calculations and crack risk
866 estimation in hardening concrete structures – State of the art,” 2011.
- 867 [54] Bureau voor Normalisatie, “NBN EN 12350-8: Testing fresh concrete - Part 8: Self-
868 compacting concrete - Slump-flow test,” in *NBN - EN*, 2019.
- 869 [55] M. Imam, L. Vandewalle, and F. Mortelmans, “Are current concrete strength tests suitable
870 for high strength concrete?,” *Mater. Struct.*, vol. 28, no. 7, pp. 384–391, 1995, doi:
871 10.1007/BF02473073.
- 872 [56] Bureau voor Normalisatie, “NBN EN 12350-6: Testing fresh concrete - Part 6: Density,”
873 in *NBN - EN*, 2019.
- 874 [57] Bureau voor Normalisatie, “NBN EN 12350-7: Testing fresh concrete - Part 7: Air
875 content - Pressure methods,” in *NBN - EN*, 2019.
- 876 [58] American Society of Testing and Materials, “Standard Test Method for Time of Setting of
877 Concrete Mixtures by Penetration Resistance,” in *Annual Book of ASTM Standards*, vol.

- 878 04, 1999, pp. 1–6.
- 879 [59] Bureau voor Normalisatie, “NBN EN 12390-13: Beproeving van verhard beton - Deel 13:
880 Bepaling van de secans- elasticiteitsmodulus bij druk,” in *NBN - EN*, no. september, 2005,
881 p. 149.
- 882 [60] Bureau voor Normalisatie, “NBN EN 12390-3 : 2019 Testing hardened concrete - Part 3 :
883 Compressive strength of test specimens,” in *NBN - EN*, 2019.
- 884 [61] SMARTEC, “Standard SOFO Deformation Sensor.” .
- 885 [62] American Society of Testing and Materials, “Standard Test Method for Determining Age
886 at Cracking and Induced Tensile Stress Characteristics of Mortar and Concrete under
887 Restrained Shrinkage,” in *Annual Book of ASTM Standards*, West Conshohocken, PA,
888 2004.
- 889 [63] Z. P. Bažant and E. Osman, “Double power law for basic creep of concrete,” *Mater.*
890 *Struct.*, vol. 9, no. 1976, pp. 3–11, 1976, doi: 10.1007/BF02478522.
- 891 [64] T. Kanstad, D. Bosnjak, and J. A. Øverli, “3D Restraint Analyses of Typical Structures
892 with Early Age Cracking Problems, IPACS report,” Sweden, 2001.
- 893 [65] B. A. Graybeal, “Material Property Characterization of Ultra-High Performance
894 Concrete,” *Fed. Highw. Adm.*, no. FHWA-HRT-06-103, p. 186, 2006.
- 895 [66] S. Smeplass, “High Strength Concrete, SP4. Material Design. Report 4.4-Mechanical
896 Properties- Normal Density Concrete,” Trondheim, Norway, 1989.
- 897 [67] M. Held, “Research results concerning the properties of high-strength concrete,”
898 *Darmstadt Concr. Annu. J.*, vol. 5, pp. 71–78, 1990.
- 899 [68] “NBN B 15-220; 1970 (NF)-Influence des Dimensions et Formes de l'éprouvette sur la
900 Résistance à la Compression du Béton,” .
- 901 [69] W. Schlee, “Die Zwangspannungen in einseitig festgehaltenen Wandscheiben,” *Beton-*
902 *und Stahlbetonbau*, vol. 57, no. 3, pp. 64–72, 1962.
- 903 [70] C. Civil Engineering and Building Structures Standards Committee, “Part 2: Code of
904 practice for special circumstances,” in *BS 8110-2: Structural use of concrete*, London,
905 UK, 1985.
- 906 [71] A. E. Klausen, T. Kanstad, Ø. Bjøntegaard, and E. J. Sellevold, “The effect of curing
907 temperature on autogenous deformation of fly ash concretes,” *Cem. Concr. Compos.*, vol.
908 109, no. January 2019, 2020, doi: 10.1016/j.cemconcomp.2020.103574.
- 909 [72] M. H. Zhang, C. T. Tam, and M. P. Leow, “Effect of water-to-cementitious materials ratio
910 and silica fume on the autogenous shrinkage of concrete,” *Cem. Concr. Res.*, vol. 33, no.
911 10, pp. 1687–1694, 2003, doi: 10.1016/S0008-8846(03)00149-2.
- 912 [73] T. Xie, C. Fang, M. S. Mohamad Ali, and P. Visintin, “Characterizations of autogenous
913 and drying shrinkage of ultra-high performance concrete (UHPC): An experimental
914 study,” *Cem. Concr. Compos.*, vol. 91, no. August, pp. 156–173, 2018, doi:
915 10.1016/j.cemconcomp.2018.05.009.
- 916